

REMOVING INTERNAL REFLECTIONS FROM DEEP IMAGING DATASETS

COLIN T. SLATER,¹ PAUL HARDING, AND J. CHRISTOPHER MIHOS
Department of Astronomy, Case Western Reserve University, Cleveland, OH.
Draft version October 31, 2018

ABSTRACT

We present a means of characterizing and removing internal reflections between the CCD and other optical surfaces in an astronomical camera. The stellar reflections appear as out-of-focus images and are not necessarily axisymmetric about the star. Using long exposures of very bright stars as calibration images we are able to measure the position, size, and intensity of reflections as a function of their position on the field. We also measure the extended stellar point-spread function out to 1° . Together this information can be used to create an empirical model of the excess light from bright stars and reduce systematic artifacts in deep surface photometry. We then reduce a set of deep observations of the Virgo cluster with our method to demonstrate its efficacy and to provide a comparison with other strategies for removing scattered light.

Subject headings: Data Analysis and Techniques

1. INTRODUCTION

Deep wide-field imaging is widely used to study extended, diffuse objects such as low surface brightness galaxies (McGaugh et al. 1995; Sprayberry et al. 1996; Marshall 2004), the diffuse interstellar medium (Sandage 1976; Gordon et al. 1998; Witt et al. 2008), the outer disks and faint stellar features around bright galaxies (Malin & Carter 1983; Pohlen et al. 2002; Martínez-Delgado et al. 2009), the diffuse intracluster light in galaxy clusters (Uson et al. 1991; Gregg & West 1998; Feldmeier et al. 2004; Gonzalez et al. 2005; Mihos et al. 2005), and the extragalactic background light (Bernstein 2007). Accurately measuring faint surface brightnesses places stringent demands on the minimization of systematic effects, including large scale flat fielding, accurate sky subtraction, scattered light from nearby objects, and internal reflections in the telescope/camera system. All of these effects, if not treated carefully, can imprint a spatially varying pattern of light onto the image, which can significantly contaminate measurements of the low surface brightness astronomical object being studied.

In particular, internal reflections of bright stars in the field represent a significant source of this type of contamination. Light coming to focus can reflect off the CCD and back up the optical path, reflect again off optical elements such as the dewar window, filter, or any reimaging optics, and come back down to the CCD. The longer path length results in multiple out-of-focus stellar images (one for each reflection) being added to the image. These defocused stars are essentially extended images of the telescope's entrance pupil, and have complex spatial structure due to obstructing objects such as the Newtonian mirror and its support spider. As we show below, the position of these reflections relative to their central star changes across the field of view, making characterization and subtraction difficult. They also complicate the measurement of the extended stellar PSF, making the subtraction of the low surface brightness wings of

stars problematic. The complex pattern of overlapping reflections and stellar wings can then plague efforts to accurately model and subtract sky from the images.

Some of this contamination can be reduced in hardware, through careful baffling of the telescope to reduce scattered light, minimization of optical elements to reduce the number of reflecting surfaces, and the use of aggressive anti-reflective coatings on the optical surfaces to reduce the intensity of the reflections. A particular example of this kind of effort is our optimization of Case Western Reserve University's Burrell Schmidt for deep surface photometry. This 24/36-inch Schmidt telescope is located at Kitt Peak and was originally designed for wide field imaging with photographic plates (Nassau 1945). The telescope was subsequently converted to Newtonian focus with a flat Newtonian mirror and a CCD imaging camera located on the side of the telescope tube.

The telescope is particularly well-suited to deep surface photometry by its original design, and in addition we have made additional upgrades to increase its sensitivity. The telescope's closed-tube design and the use of a Newtonian focus severely limits the amount of stray light that reaches the detector. Recent upgrades to the telescope include a redesign of the Newtonian mirror and its mounting structure to reduce vignetting and flexure, an installation of light-absorbing material to the inside of the telescope tube to reduce scattered light, the installation of a wide field 4Kx4K CCD ($1.65^\circ \times 1.65^\circ$ on the sky), a combining of the dewar window and field flattener to reduce optical surfaces, and the use of filter-specific anti-reflective coatings on the filter and dewar window/field flattener (see Appendix A). With these improvements, the telescope has been able to detect extremely faint structure in the intracluster light of Virgo (Mihos et al. 2005).

However, in practice many of these solutions are generally unavailable to the observer on a multi-user, multi-instrument telescope, and even with such solutions in place, faint reflections still persist. In these situations, software solutions must be implemented to correct for these reflections in the reduction process, after the data has been taken. In this work we present a way of

Electronic address: colin@astronomy.case.edu, paul.harding@case.edu, mihos@case.edu

¹ now at the Department of Astronomy, University of Michigan

characterizing and removing these reflections in post-processing. This provides a cost-effective way to increase the telescopes ability to image very faint structure. Modeling the reflections in software is also convenient in that it does not require any modification to the telescope or other work on the part of the instrument scientist, and can be implemented by an observer without the aid of the observatory staff. The only change necessary to the observing program is the observation of a small number of bright stars in order to characterize the sizes, intensities, and positions of the reflections. With this information a generative model of the reflections can be built and used to remove the scattered light.

The outline of our paper is as follows. In §2, we characterize the reflections from our Schmidt imaging data and show that they are as expected for the optical design of the telescope. We also describe a process for removing them from the images. In §3, we use the reflection subtracted images to accurately measure the point spread function of the telescope out to 1° . In §4, we examine the scientific impact of the technique by comparing the results of our deep imaging of Virgo with and without the full reduction technique in place. Finally, in §5 we present a step-by-step “cookbook summary” of the technique and suggest avenues by which the technique could be further improved.

2. CHARACTERIZING THE REFLECTIONS

An example of these reflections as seen in the Burrell Schmidt can be seen in a long observation of Arcturus, shown in Figure 1. Along with a completely saturated stellar core and strong bleeding as expected, we can see scattered light from the star covering the entire field of view of the detector. The images also show a bright annulus of light around the star extending out to a radius of 17 arcminutes. A schematic drawing of the reflections giving rise to this feature is shown in Figure 2. In all of these images the bright ring around the star is caused by specular reflection of light from the star off the CCD, which then travels back up to the filter and is reflected again onto the CCD. The reflected light creates an out-of-focus image due to the additional path length. This image shows the shape of the telescope pupil, which is the round aperture of the telescope with a shadow cast by the Newtonian mirror and its support structure. There are also similar reflections from other optical surfaces in the telescope, including the top and bottom of the dewar window and the top surface of the filter. All of the reflections we observe involve the CCD as one of the reflecting surfaces since its 10% average reflectivity is significantly higher than either the dewar window or the filter.

The observed reflections are not concentric about the star for a number of reasons. The reflections are shifted radially from the optical center of the focal plane due to the star’s angle of incidence on the detector. Any inclination of the CCD with respect to the focal plane, or any curvature to the CCD itself will also cause reflections to be offset. In the Burrell Schmidt the effect of the star’s angle of incidence is the dominant cause of the offset, and the reflections are shifted radially inwards toward the optical center. In a Schmidt telescope the light cone for an off-axis star comes from only a portion of the primary mirror, since the entrance pupil is defined by the corrector lens on the telescope and not the mirror. Since the

light from a star comes to the detector from a region on the primary mirror that is further away from the optical center, the reflected light will be shifted inwards towards the center of the field. Figure 2 shows a schematic view the reflection from an off-axis star, with the light cone first coming to a focus on the CCD and reflecting first off the CCD and then the filter. The resulting image is drawn below the CCD and shows the relative position of the star and the annulus (the drawing is significantly exaggerated for illustrative purposes).

To characterize the reflections seen on images, we observed a series of sixteen 450-second exposures of the bright star Arcturus ($M_V = -0.05$) with the Burrell Schmidt under photometric conditions. For each of these images the star was positioned in a different portion of the detector, so that the set of images evenly covered the field of view. The images were bias subtracted and flat fielded using a sky flat. The sky flat was generated using over 50 sky pointings interleaved between science exposures (see, e.g., Morrison et al. 1997; Mihos et al. 2005). The images were photometrically calibrated using stars from the Sloan Digital Sky Survey that were in the field of view. All data were taken with the Washington M filter, which was chosen to minimize the contribution of sodium lines from street lights at 589 nm and the O I airglow line at 557 nm (see Feldmeier et al. 2002, Fig. 1). The detector used is a 4096×4096 pixel CCD that was thinned and packaged by the University of Arizona’s Imaging Technology Laboratory (ITL). An anti-reflective coating was also applied to the detector by ITL. On the telescope the detector has a pixel scale of $1''.45 \text{ pixel}^{-1}$ for a field of view of $1^\circ.65 \times 1^\circ.65$.

A composite radial profile is shown in Figure 3, using 450 second exposures of Arcturus for the region beyond ~ 2 arcminutes, 10 second exposures of Arcturus for the region between 0.2 and 2 arcminutes, and a faint star for the innermost region of the profile. There are numerous peaks caused by reflections within various optical elements; the most obvious extend from 0.7 to 2.0 arcminutes and are caused by a reflection within the Schmidt corrector. This reflection is strongly distorted by the complex curvature of the corrector and we do not attempt to characterize it. Bright stars will be masked from the science images out to ~ 2 arcminutes in order to eliminate all of these features. The corrector is also responsible for the “Schmidt ghost,” which is a diffuse image that appears reflected across the optical axis from bright stars. The ghost is the result of light from a star reflecting off the CCD, travelling back up the telescope, reflecting off the corrector, and ultimately returning to the CCD. This ghost was masked out of all calibration and science images. The most distinct reflections beyond 2 arcminutes are caused by the dewar window and the filter, and appear as bumps in the PSF at roughly 2.5 and 10 arcminutes from the star. These are the reflections that will be modeled and removed.

The sources of the reflections can be confirmed by using the size of the reflections to determine the extra path length traveled by the reflected light. The size of the two largest reflections correspond to a reflecting surface 3.6 cm away from the CCD, which matches the position of the filter. The bottom surface of the filter (the side closest to the CCD) causes the brightest reflections,

and can be easily seen in all the example images. The top surface of the filter produces a much fainter reflection, which is barely apparent (see Figure 4) as a ring slightly beyond the bright annulus of the bottom surface's reflection. There is also a reflection off the bottom surface dewar window, which lies between the CCD and the filter, and a fainter reflection off the top of the dewar window. The size of the bottom reflection indicates that the window is 0.6 cm away from the CCD as expected. The reflection off the top of the dewar window was faint enough to be far below the noise level on realistic foreground stars near the science fields, and so we do not attempt to model it. Similarly multiple bounces between the reflecting surfaces and the CCD will contribute a small amount of light at large radii, but using the measured reflectivities we calculate that all of the secondary reflections will have surface brightnesses fainter than $\mu_V = 30 \text{ mag/arcsec}^2$ in our Arcturus images, well below our detection limit. A summary of the reflecting surfaces and the brightness of their reflections is presented in Table 1.

These reflections have been modeled in Zemax, an optical ray-tracing program, to confirm their source and the causes of the offset between stars and their reflections. The model of the telescope included all optical surfaces in the light path, including the Schmidt corrector plate, primary and Newtonian mirrors, filter, dewar window, and CCD. In the Burrell Schmidt there is also a contribution to the shift from the convex curvature of the detector, which is on the order of a $100 \mu\text{m}$ height difference between the center and the edges of the CCD. The measurement of the curvature was obtained from focus images, where we found the focus position that produced the smallest star profiles in each corner and in the center of the chip. Using this information we were able to calculate the expected centers of the reflections, and therefore their offset from the star. The ray-tracing found reflection centers that matched the observed positions to within ten pixels, without accounting for any inclination of the filter or CCD.

Using observations of Arcturus to measure the offset between the center of the star and the center of its reflection we determined that the offset could be modeled as a linear function of position on the detector. For instance, a star on the optical axis has concentric reflections, and as one moves away from the axis the distance between the star and the center of its reflection increases linearly. Combining fits of the offset as a function of row and of column on the detector can account for both radial shifts (caused by the angle of incidence) and linear shifts (caused by tilts of the optics or detector).

The measured offsets of the reflections are plotted in Figure 5. The bottom of the filter and the dewar window reflections are both shown. This confirms that the shifts are a linear function of position, and that the curvature of the CCD has not added a significant nonlinear component as one would expect from an extremely concave or convex detector. The figure also shows that the offsets can be measured empirically simply using bright-star observations that cover the field of view. Although ray-tracing was helpful in confirming our understanding of the behavior of the telescope, it is not necessary for modeling the reflections.

To determine the brightness of the reflections, we first

roughly measured the difference in brightness between regions just inside and just outside the edge of the reflection with IRAF's *imexam* tool. We then recalculated the radial profile after subtracting off the reflection to see if any evidence of the reflection could still be seen. This first estimate was further refined by making small changes to the fraction of light reflected that our model specified, then repeating the process of applying the reflection removal and calculating the resulting radial profile. We continued to adjust the reflection in this way until the profile was featureless around the area of the reflection we were removing. This process was performed for a single image, then the results were applied to all of the other observations using the same value of the fraction of reflected light. The resulting profiles in the other images also showed no features in the reflection region, which indicates that our reflectivity measurement is not biased by only using one image in the process. This also indicates that the reflectivity of the various optical surfaces is position-independent to within our errors.

To summarize our parameters, each reflection is modeled by an offset from the star, which is a linear function of both row and column on the detector, a constant circular size, and a brightness, which is the fraction of the total intensity of the star that reaches each pixel in the reflection area.

We determined these parameters for three surfaces in the Burrell Schmidt: the top and bottom surfaces of the filter and the bottom surface of the dewar window. All of the reflections also have an inner shadow in the center caused by the obstruction of the pupil by the Newtonian mirror. The position of the shadow can be modeled in the same way as the other reflections. The reflection from the bottom of the filter shows this shadow most clearly. However, the shadows from the filter top and dewar window bottom reflections are not visible in our Arcturus observations since they are both very faint relative to the profile of the star at their respective radii. The inner edge of the dewar window reflection is close enough to the star that it will be masked, and the oversubtraction of the extremely faint filter-top reflection will be negligible in the inner regions of the profile.

Figure 6 shows the result of removing the reflections from the images of Arcturus shown in Figure 4. The reflections are completely removed except for some small amplitude rings and the shadows caused by the spider supporting the Newtonian mirror. These faint structures will be smoothed out by coadding multiple dithered images, since in each image the structures will have moved slightly.

The radial profile before and after removing the reflections can be seen in Figure 7. The upper line shows a mean of the uncorrected radial profile of the sixteen bright star images, while the middle dotted line shows the mean of profiles after removing the reflections from the individual images. The shaded area shows the scatter between the images, and extends between the maximum and minimum intensity of the sixteen profiles at a given radius. The profiles are photometrically calibrated with other stars in the field and are not affected by the saturation of the core of Arcturus. The regions of the profile corresponding to removed reflections are indicated by the horizontal lines at the top of the Figure 7. These are not necessarily the exact positions of the removed features,

since the reflections are offset from the center of the star and hence are not radially symmetric about the star. This also causes the radial profile to show a smooth transition instead of the sharp cut-off at the reflection edges as seen in the images.

3. ATMOSPHERIC AND INTERNAL SCATTERING

After removing the modeled reflections from each pointing, our bright star images were coadded to obtain a mean point-spread function for all positions on the detector, which is shown by the middle line in Figure 7. We expect that point-spread function after reflection removal to be independent of position in the field of view. This is attested by the small scatter between the profiles of the different pointings, as shown by the light gray shading.

The PSF can be divided at 5 arcminutes into two regions with significantly different behavior. Inside of 5 arcminutes the behavior of the profile is determined by the effects of diffraction, turbulent scattering in the atmosphere, and complex internal reflections in the corrector. In this region the profile exhibits a steep dependence on distance from the star that becomes shallower further out. Approximating different parts of the profile inside of 5 arcminutes as power laws produces varying results, with power law slopes ranging from -3 to -2.4.

Inside of 10 arcseconds the profile should be dominated by the behavior of turbulent scattering in the atmosphere, along with diffraction. Assuming the turbulence follows Kolmogorov statistics this inner PSF should be fit by a Moffat function (Racine 1996). However, in our data the $1''.45$ pixels do not adequately sample the PSF in this inner region and we can only observe the outer wings of the turbulent scattering.

Between roughly 10 and 200 arcseconds a number of bright reflections appear in the profile. These reflections are caused by multiple bounces within the corrector lens, and exhibit complex and varying shapes due to the figuring of the corrector. This part of the radial profile has been measured in many other telescopes with results often indicating an r^{-2} behavior (King 1971; Surma et al. 1990; Racine 1996) or slightly steeper (Gonzalez et al. 2005; and see Bernstein 2007 for a more complete review). Our measurements find a steeper behavior than r^{-2} and closer to $r^{-2.4}$. The complex reflections make it difficult to determine the source of this steep profile. We do note that diffraction would show a steeper profile, since the light from diffraction by an annular aperture falls off as r^{-3} . Despite this rapid fall-off, the light from diffraction can still be significant at radii up to an arcminute or more. Note that the sharp diffraction spikes caused by the Newtonian spider structure are not the issue here; those spikes are masked out of the radial profile.

Beyond 5 arcminutes the PSF begins to fall off less rapidly, and can be fit roughly with a power law of index -1.6. Few measurements of the PSF on other telescopes extend out to these radii. King (1971) finds a power law index of -2 at these radii. King refers to the r^{-2} behavior as the aureole. There is no consensus as to the source of the aureole, though there has been speculation about scattering due to dust, microripples in the primary mirror, and multiple-bounce diffuse reflections (Racine 1996).

Similarly we cannot provide any confident explanation of the $r^{-1.6}$ behavior we observe. One hypothesis could be that improper background subtraction lead to a bias in the profile, but this cannot be supported. While the behavior of the PSF beyond ~ 20 arcminutes is sensitive to improper background subtraction, the region inside of 20 arcminutes should be dominated by scattered light from the star. At 10 arcminutes from the star, our 5 ADU uncertainty in the background subtraction will vary the profile by less than 0.01 magnitudes, while at 40 arcminutes the uncertainty in the background subtraction contributes to an uncertainty of 0.1 magnitudes. It is therefore unlikely that the $r^{-1.6}$ behavior could be an artifact of the background subtraction.

Regardless of the source of the scattered light, we model the point spread function with a third-order polynomial in log space, fit to the mean PSF between 2.4 and 60 arcminutes. This region contains 1.2% of the total light from the star, which is roughly consistent with measurements made at other telescopes (Bernstein 2007). Beyond one degree the amount of light from Arcturus becomes difficult to distinguish from the sky background. Since no science fields are close enough to a star as bright as Arcturus to cause significant contamination at these radii, we are not concerned with modeling beyond one degree.

The result of subtracting the PSF can be seen as the bottom line of Figure 7. The line indicates the profile after coadding all of the filter- and PSF-subtracted Arcturus observations, while again the gray region delimits the spread of the profile from individual images. This coadd approximates the behavior one would see in images produced by coadding dithered observations, which will smooth out any remaining high spatial frequency features in the stellar profile.

In modeling the PSF we chose to be somewhat cautious about avoiding oversubtraction. At any given radius the observed profile of a single star will have some scatter which will be asymmetric around the mode, in the sense that there are more likely to be features with positive intensities (e.g. nearby stars in the field or the star's faint diffraction spikes) or than features with negative intensities (e.g. read noise, which is symmetric). Because of this our fit was designed to err on the side of undersubtracting, and as a result the subtracted PSF in Figure 7 still shows some positive features such as diffraction spikes inside of 5 arcminutes.

4. SCIENCE REDUCTION

In order to assess the systematic biases and artifacts introduced by different methods of star subtraction we have reduced deep observations of the Virgo cluster with both our PSF modeling technique and other more common methods, including using no star subtraction and subtracting a static PSF. In many situations, including point source photometry and localized surface photometry, the scattered light contribution from nearby stars is often ignored and treated as a generic background. This is reasonable in these situations because the variability in the PSF as a result of reflections only affects a very small fraction of the total light from the star. Nearby stars are also often ignored when measuring the total integrated magnitude of a galaxy, for much the same reason. In faint extended surface photometry, such as isophote fit-

ting of galaxies, star subtraction is usually performed with a PSF that is static across the field of view. This can be a reasonable assumption for telescopes with small fields-of-view in which the PSF does not vary much, but with very large detectors modeling of the variable PSF becomes much more important.

To compare the effectiveness of our modeling to other reduction strategies we have performed a series of reductions on deep observations of the Virgo cluster. We observed a region near the center of the Virgo cluster for eight nights under photometric conditions and no moon, obtaining 52 science exposures of 900 seconds each in the Washington M filter. The images were bias subtracted, flattened with the same flat as had been used for the Arcturus data, and the magnitudes were transformed to Johnson V magnitudes. We then developed a catalog of stars in and near the target field from the Tycho 2 and SDSS databases. For every image we selected all the stars from these catalogs within 72 arcminutes of the center of the image and constructed a model PSF for each star, scaled to the star's total flux. For stars that fell onto the detector, we also constructed a model image of the reflections generated by each star. We coadded all of the model PSFs and reflections to obtain an image of the total scattered light in a field, and we subtracted this image from the science observation.

After removing the scattered light, we sky-subtracted the images using the method described by Mihos et al. (2005). In this technique the images were registered, then a sky image was constructed from each one by masking out all objects. Planes were fit to the individual sky images and an iterative procedure adjusted the planes in order to minimize the discrepancy between exposures after removal of the sky planes.

The resulting mosaic of the Virgo cluster is shown on the right side of Figure 8. Much of the eastern region of the mosaic is contaminated by high-latitude galactic dust, which reflects light from the Galactic disc (e.g., Sandage 1976; Witt et al. 2008). It is unlikely that any of the green-colored structure in this area is intracluster light. Faint ICL structures can indeed be seen emanating from M87, as was previously observed in Mihos et al. (2005).

To emphasize the impact of the scattered star light we performed one reduction of the data without any reflection removal or star subtraction. This is shown on the left in Figure 8. The difference between the properly star-subtracted image and the reduction without star subtraction is shown in Figure 10. The most significant contribution to the excess light comes from three eighth-magnitude stars to the west of M87. In total, the flux from foreground stars in the field is equivalent to a single star of magnitude $M_V = 3.7$. As discussed in §3, since at least 1.2% of the star light is scattered to radii beyond $2.4'$, there is significant diffuse light across the entire field. Figure 9 shows the fraction of the mosaic contaminated by scattered light at a given level. This shows that 50% of the image has scattered light at the $\mu_V = 28.8$ level, and 10% receives more than $\mu_V = 28.0$ of scattered light.

This excess light not only limits depth to which we can detect faint structure, but also strongly biases the background subtraction. Because we fit planes to individual images, the plane-fitting will attempt to remove

the excess light from stars in the mosaic center. This distorts the background planes and significantly degrades the accuracy of the background subtraction in the outer parts of the mosaic. This has the potential to distort isophotes in the outer regions of galaxies where proper background subtraction is crucial. In the images shown we subtract the same background planes from both reductions in order to ease comparison between the two. Even with the proper background subtraction the outer regions of M87 show considerable variation between the two reductions. Toward the southern end of M87 the image without star subtraction shows the galaxy extending much further than the star-subtracted image. Any attempts to measure the galaxy's profile at these distances must therefore carefully account for scattered light effects.

The improvement in the final mosaic made by modeling the reflected light is perhaps not as dramatic in the Burrell Schmidt as it would be in telescopes that are less optimized for deep surface photometry. The anti-reflective coatings on the optics in the Burrell Schmidt significantly reduce the reflected light compared to other optical telescopes, including many large multi-user facilities. The reflectivities of the optics in the Burrell Schmidt are all less than 0.8%, while reflectivities around 2 - 4% are much more common. We have attempted to emulate the images that would be produced by a telescope with higher-reflectivity optical components by using our model to generate the additional light that would be reflected. We add this to the science observations to obtain an image that is more representative of what would be observed on an unoptimized telescope. Without any star subtraction the image with bright reflections shows an excess of light of almost 7 ADU around regions with bright stars, and on average an excess of 4 ADU spread diffusely across the mosaic. This diffuse component is equivalent to a surface brightness of $\mu_V = 28.0$ mag arcsec⁻².

Although the reductions without star subtraction make the most dramatic comparison, it is not representative of common practice in deep surface photometry. The most widely used method of treating foreground stars is to subtract a PSF that is static across the field of view. We investigate the biases and artifacts caused by this technique by using our images with the exaggerated reflections and subtracting a mean, static PSF from each star.

This static profile creates significant errors near the edges of the reflections around each star, and has the potential to mimic sharply-defined tidal structures in adjacent galaxies. A comparison between different PSF subtraction methods is shown in Figure 11, which uses sixteen dithered exposures of Arcturus. In the top panel a normal coadd is shown with no star subtraction. The left panel shows the coadd after subtracting a static profile from each image, and the right shows Arcturus after subtracting modeled reflections from each exposure. The bright ring in the left image is illustrative of the artifacts that using a static PSF can introduce. The ring has the same brightness as the filter reflection. The artifacts of static-PSF star subtraction can also be seen in a mosaic of the Virgo observations. Figure 12 shows a region around M87 where a bright star has caused a ring which, though faint at the ~ 1 ADU level, could easily mimic a tidal feature. While such spurious features might be

recognized by their proximity to a bright star, more complex structures due to the overlapping wings of a number of stars might be more difficult to clearly identify as artifacts.

One concern that can be raised about our method is that we only correct for scattered light from bright stars in the field, while bright galaxies will also contribute scattered light. This contribution can be significant since, for example, the integrated V magnitude of M87 is 8.63 (de Vaucouleurs et al. 1991), which is comparable to some of the brighter stars in our field. The most technically correct method of accounting for this scattered light would be to deconvolve the images with our spatially varying model for the reflections and the PSF, but this is an extremely computationally-intensive operation. Instead, we simply estimate the severity of the effect by calculating the scattered light received at a given pixel as if the original image was a true measure of the light distribution in the field (unaffected by scattering).

We can perform this estimation using M87 as an example. At the a radius of $10'$ from the center of M87, similar to the distance to the NGC 4476/4478 to the west, the scattered light has a surface brightness of roughly $\mu_V = 26.7$. Subtracting this excess light from the measured surface brightness of $\mu_V = 25.8$ at $10'$ along the minor axis results in a change of roughly 0.5 magnitudes. Further out at $15'$ the scattered light falls to $\mu_V = 28.5$, which would lead to a 0.2 magnitude correction in the measured surface brightness at that distance along the minor axis. At even larger radii from the galaxy the scattered light quickly falls below the noise threshold. Thus in our observations of the ICL we can safely ignore the scattered light from galaxies, but observing programs that focus on the light profiles of galaxies themselves at intermediate radii may require a more careful treatment (e.g. de Jong 2008).

5. SUMMARY AND APPLICATION

We have presented a method for characterizing and removing reflections and scattered light in the post-processing of images. We found that reflections off of the CCD produce annular rings in the images after they reflect back off of either the filter or dewar window. The rings are circular and are uniform in their brightness to roughly 5%, and are not necessarily axisymmetric about the central star. However, the offset between the star and the center of the rings is a linear function of the star's position on the detector. Using this information we build a model for the reflections and the diffuse scattered light from each star and use it to remove this excess light from our observations of the Virgo cluster.

By comparing our reduction techniques to other methods we have shown that star subtraction is critical for faint surface photometry. Omitting star subtraction from the reduction, even on an optimized telescope, will create significant errors in background subtraction and will distort the appearance of the outer regions of galaxies. We have also shown that performing star subtraction with a PSF that does not vary over the field of view can be a reasonable reduction method, but runs the risk of creating artifacts that look conspicuously like tidal structures. Modeling the changing PSF across the field is the safest way to ensure that these artifacts do not appear.

Porting this method to other telescopes requires three main sets of calibration observations: a set of bright star observations across the field of view to measure the behavior of the reflections in an instrument, one or more deep observations of a bright star to measure the smooth component of the extended PSF, and a small number of periodic checks during an observing run to confirm the stability of the reflections.

The first step in developing the reflection model is to obtain 10-16 bright star observations to ensure that the reflections in a particular instrument and telescope are linearly related to the position of the central star. These exposures only need to be long enough to make the reflections visible. Ray tracing could be used to confirm the linear behavior of the reflections, but in most instruments it cannot substitute for the empirical measurements of the reflection offsets. To obtain the required accuracy from ray tracing, assuming spacings of a few centimeters between the CCD and the reflecting surfaces, the surfaces would need to be aligned to within one to two arcminutes of the optical axis. For a four-inch filter this would mean that the filter could only deviate $100 \mu m$ from parallel. In instruments where these tolerances are not met the only reliable way to measure the reflection locations is with bright star observations.

Once it is known that the reflections behave linearly in an instrument, the locations of the reflections only need to be checked periodically throughout an observing run with a small number of bright star observations. These observations also do not need to be very long, but should be performed at least once per observing run, if not more frequently.

Longer observations are needed to measure the smooth component of the extended stellar PSF, but fewer exposures are necessary since this component of the PSF should not vary across the field of view. These observations can be performed much less frequently than the reflection checks, and it should only be necessary to repeat them when significant changes to the optics are made, such as realignment of the mirrors or changes of the filters or optics.

It is also important to underscore the importance of dithering observations of a field when attempting to perform surface photometry. Throughout this work we have demonstrated the complex structure of the instrumental PSF (speaking broadly to include the reflections) and the variation it exhibits across the field of view. Though we can successfully remove the brightest components of this structure, we still rely on dithering to average out smaller scale features such as the shadow of the Newtonian spider and the rings caused by the corrector. For this to be effective the movement between exposures needs to be on the order of the size of the features to be removed. This ensures that the features move relative to the star enough to average out instead of adding constructively. Dithers of only a few pixels, as are commonly used for the drizzle routine, will likely be ineffective at reducing reflection artifacts.

It is worth reiterating the simplicity of the assumptions we have made. Two physical insights are at the center of the process: reflections are out-of-focus images, and out-of-focus images exhibit the illumination pattern of the telescope aperture. The curvature and inclination of the various reflecting surfaces only cause small per-

turbations to this image, resulting primarily in spatial shifts. We have found that linear modeling is sufficient for removing these artifacts from simple direct imaging applications, and that the resulting improvements in low surface brightness imaging is worth the extra observing

and data reduction effort.

This research was supported by the NSF through grants ASTR 06-07526 and ASTR 07-07793 to J.C.M.

APPENDIX

HARDWARE UPGRADES TO THE BURRELL SCHMIDT

Though in this work we are primarily concerned with improving the sensitivity of the Burrell Schmidt with software, numerous upgrades to the telescope hardware have also played a significant role in the optimization of the telescope for deep surface photometry.

One of the telescope's main strengths is its simple optical layout. Since the camera is a direct-imager, there are only three transmissive optical elements in the light path: the corrector lens at the top of the tube, the filter, and the dewar window. The dewar window also serves as a field flattener, which alleviates the need for another lens. Compared to the number of components needed for a reimaging camera, this setup significantly reduces the number of reflections that would need to be modeled and removed. The filter and dewar windows also have antireflective coatings which further reduce the amount of scattered light. The filter was produced and coated by Barr Associates, with a specification for a reflectivity less than 0.5%.

The telescope's closed tube significantly reduces the amount of stray light that reaches the detector. In an open-tube Cassegrain design, light from outside the field of view can reach the detector directly as long as it avoids the secondary mirror. To prevent this most telescopes have baffling around the secondary mirror to reduce this light path, but this reduction in the sky background comes at the cost of vignetting mirror aperture. Many Cassegrain telescopes also have a tube protruding from the center of the mirror which also cuts down on the stray light, but with the same vignetting problems. Properly done, the baffling should eliminate any direct path to the sky. The Nasmyth and prime foci also require baffling to prevent direct light from the dome or mirror cell from reaching the detector. Even with this baffling there exist paths where light can reach the detector after a single bounce off of the various surfaces.

In contrast the Schmidt telescope with a Newtonian focus has no direct path for light to reach the detector, nor any single-bounce paths. To further limit the possibility of stray light reaching the detector the inside of the telescope tube has been covered with light-absorbing flocking, a fuzzy velvet-like material.

Another upgrade made to the telescope in the past several years has been the replacement of the Newtonian mirror and its mount. The previous Newtonian mirror had been undersized and vignetted the field of view. The mirror had also been supported by a structural element attached to one side of the telescope tube. This element would flex and cause the vignetting to change depending on the position of the telescope. This changing illumination pattern posed a problem for flat-fielding the detector and would have also affected the accuracy of our reflection modeling. This support element was replaced with a spider structure which is connected to four sides of the telescope tube, thus reducing the flexure of the mirror. A properly-sized Newtonian mirror was also installed at the same time.

REFERENCES

- Bernstein, R. A. 2007, *ApJ*, 666, 663
 de Jong, R. S. 2008, *MNRAS*, 388, 1521
 Feldmeier, J. J., Mihos, J. C., Morrison, H. L., Rodney, S. A., & Harding, P. 2002, *ApJ*, 575, 779
 Feldmeier, J. J., Mihos, J. C., Morrison, H. L., Harding, P., Kaib, N., & Dubinski, J. 2004, *ApJ*, 609, 617
 Gonzalez, A. H., Zabludoff, A. I., & Zaritsky, D. 2005, *ApJ*, 618, 195
 Gordon, K. D., Witt, A. N., & Friedmann, B. C. 1998, *ApJ*, 498, 522
 Gregg, M. D., & West, M. J. 1998, *Nature*, 396, 549
 King, I. R. 1971, *PASP*, 83, 199
 McGaugh, S. S., Schombert, J. M., & Bothun, G. D. 1995, *AJ*, 109, 2019
 Malin, D. F., & Carter, D. 1983, *ApJ*, 274, 534
 Marshall, J. J. 2004, Ph.D. Thesis,
 Martínez-Delgado, D., Pohlen, M., Gabany, R. J., Majewski, S. R., Peñarrubia, J., & Palma, C. 2009, *ApJ*, 692, 955
 Mihos, J. C., Harding, P., Feldmeier, J., & Morrison, H. 2005, *ApJ*, 631, L41
 Morrison, H. L., Miller, E. D., Harding, P., Stinebring, D. R., & Boroson, T. A. 1997, *AJ*, 113, 2061
 Nassau, J. J. 1945, *ApJ*, 101, 275
 Pohlen, M., Dettmar, R.-J., Lüticke, R., & Aronica, G. 2002, *A&A*, 392, 807
 Racine, R. 1996, *PASP*, 108, 699
 Sandage, A. 1976, *AJ*, 81, 954
 Sprayberry, D., Impey, C. D., & Irwin, M. J. 1996, *ApJ*, 463, 535
 Surma, P., Seifert, W., & Bender, R. 1990, *A&A*, 238, 67
 Uson, J. M., Boughn, S. P., & Kuhn, J. R. 1991, *ApJ*, 369, 46
 de Vaucouleurs, G., de Vaucouleurs, A., Corwin, H. G., Jr., Buta, R. J., Paturel, G., & Fouque, P. 1991, Volume 1-3, XII, 2069 pp. 7 figs.. Springer-Verlag Berlin Heidelberg New York,
 Witt, A. N., Mandel, S., Sell, P. H., Dixon, T., & Vjih, U. P. 2008, *ApJ*, 679, 497

Reflection Surface	Distance to surface (cm)	Reflectivity	Reflection Radius (arcmin)	Surface Brightness (mag arcsec ⁻²)
Dewar window bottom	0.64	0.4%	2.7	20.7
Filter bottom	3.3	1.6%	17.0	23.0
Filter top	4.2	0.2%	19.5	25.2

TABLE 1

SUMMARY OF THE REFLECTIONS THAT ARE MODELED AND REMOVED. THESE NUMBERS USE A CCD REFLECTIVITY AVERAGED OVER THE FILTER PASSBAND OF 10% (M. LESSER, PRIVATE COMMUNICATION). THE LISTED SURFACE BRIGHTNESS IS FOR A 450 SECOND EXPOSURE OF ARCTURUS ($M_V = -0.04$).

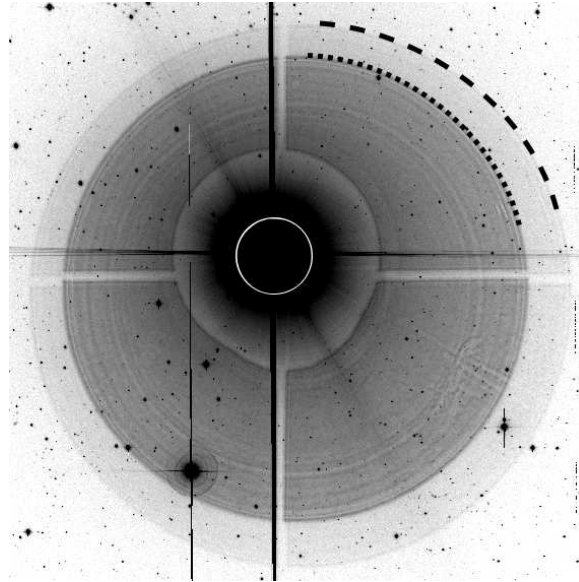


FIG. 1.— An example image of Arcturus, scaled logarithmically. The black dashed arc indicates the outer edge of the reflection off the top surface of the filter, and the dotted arc indicates the edge of the bottom surface filter reflection. The solid white circle in the center shows the extent of the dewar window reflection, which is not visible under this scaling. The image is $41' \times 41'$.

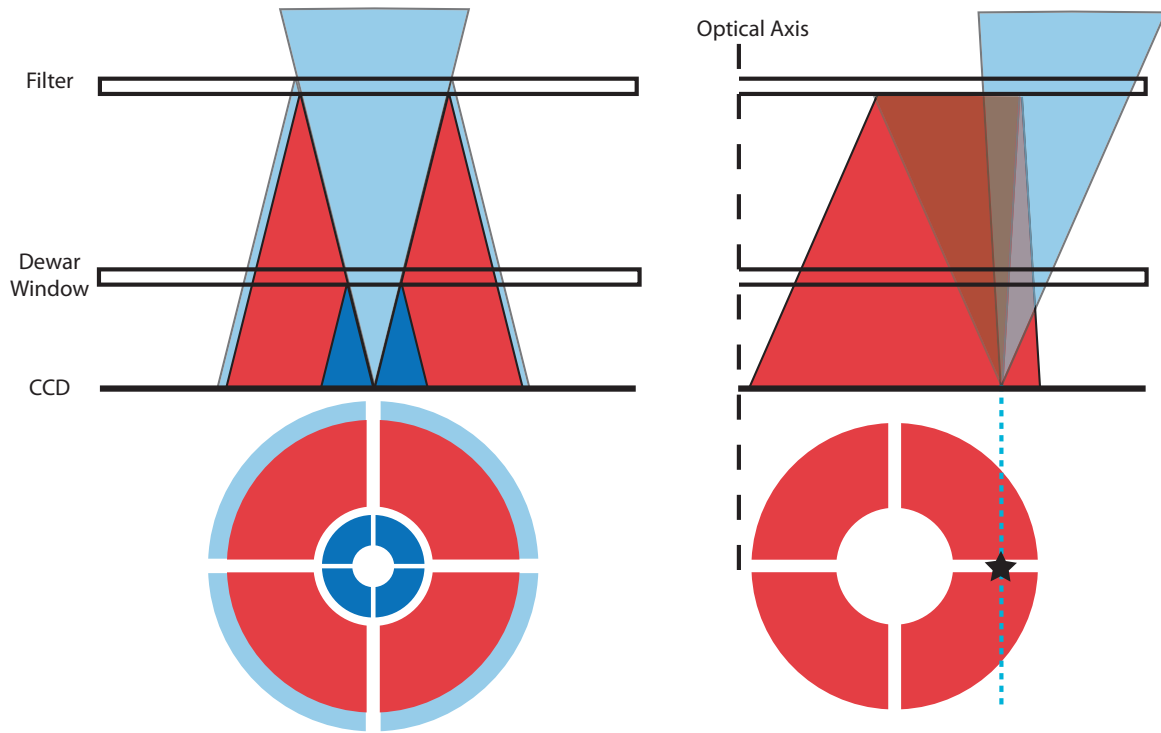


FIG. 2.— Schematic view of the surfaces causing the observed reflections. The drawing on the left is for a star in the center of the field of view, where the reflections are concentric about the star. The right drawing shows an off-axis star, which in a Schmidt telescope produces a reflection that is shifted in towards the optical axis. The appearance of the reflections on the detector is depicted below the CCD. The drawings are not to scale.

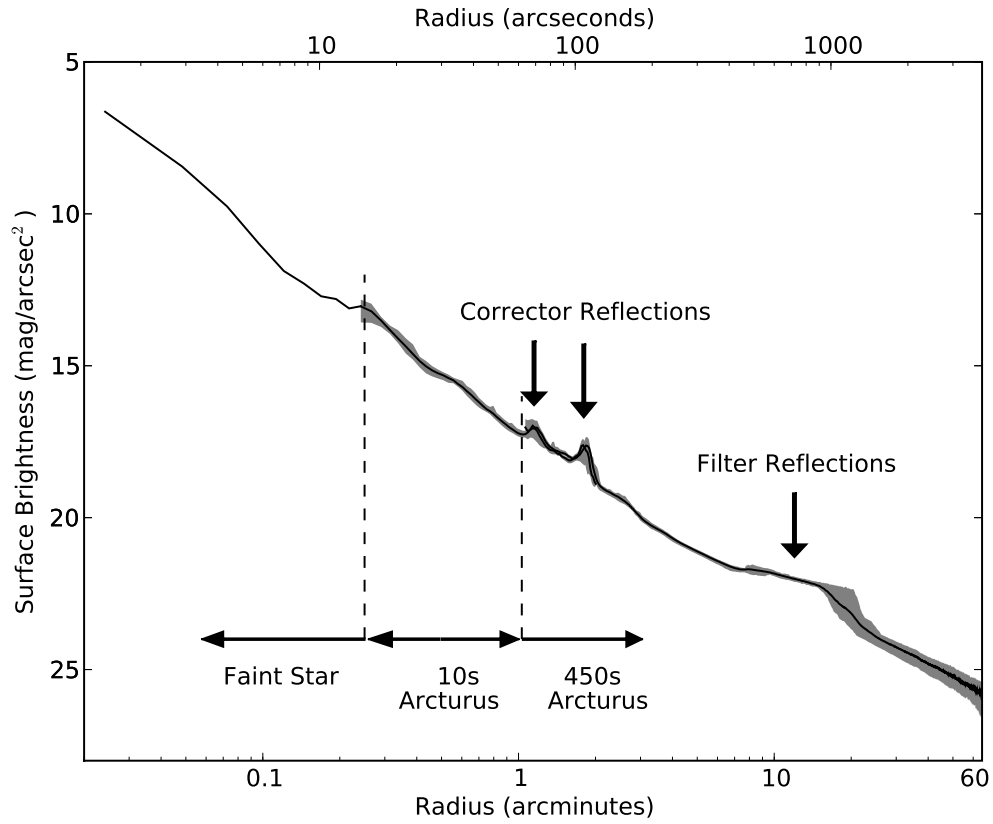


FIG. 3.— Radial profile of Arcturus out to one degree. The profile is a composite of the mean of the 450 second Arcturus exposures, the mean of the 10 second Arcturus exposures, and a faint background star. The dashed vertical lines indicate which observations were used to generate the profile in a particular region. The shading shows the variation of the PSF between different positions in the field of view.

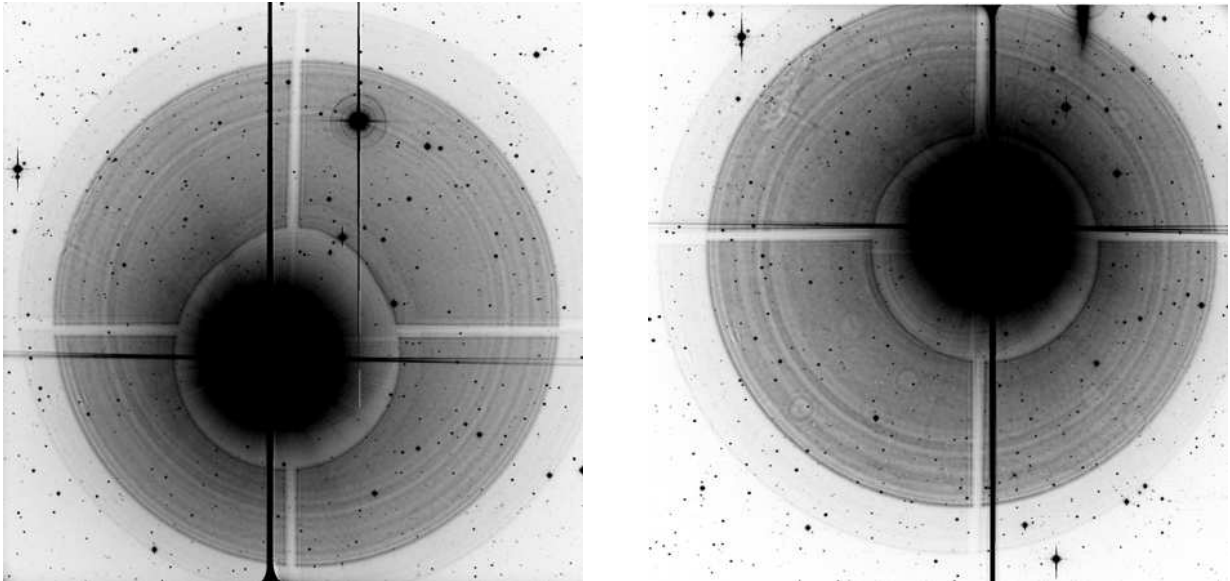


FIG. 4.— Two 450-second exposures of Arcturus, with the star positioned in opposite corners of the field of view. The optical center is towards the top right of the image on the left, and towards the bottom left on the right image. The images saturate to black at $\mu_V = 21.2$.

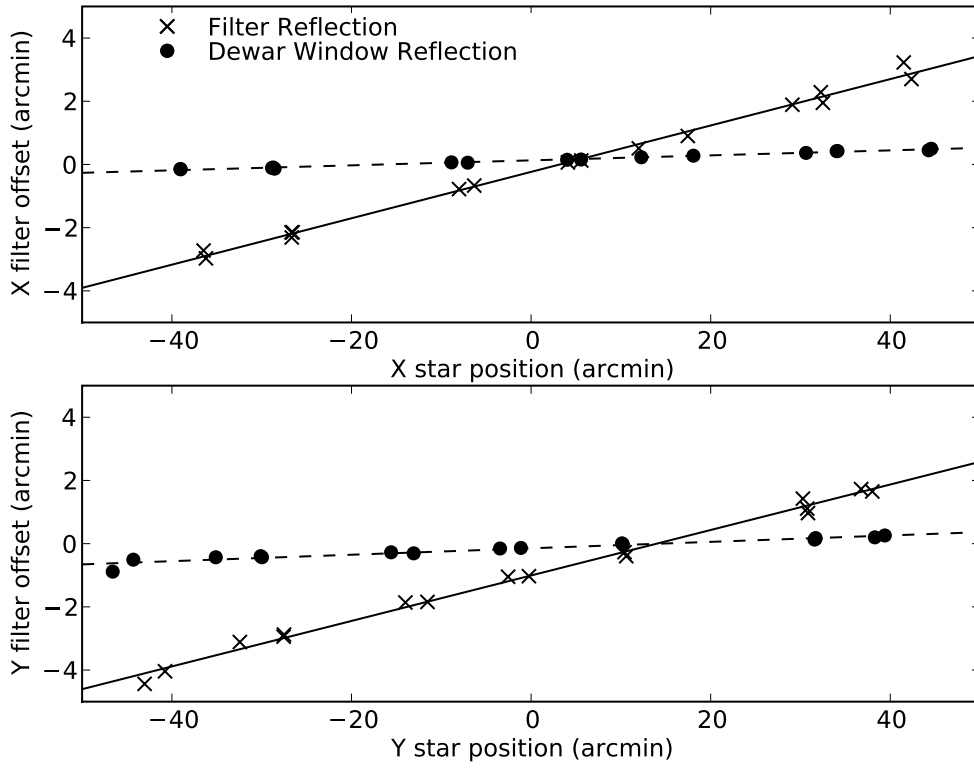


FIG. 5.— Offsets of the reflections from the star in x and y coordinates over the field of view. The solid and dashed lines are linear fits.

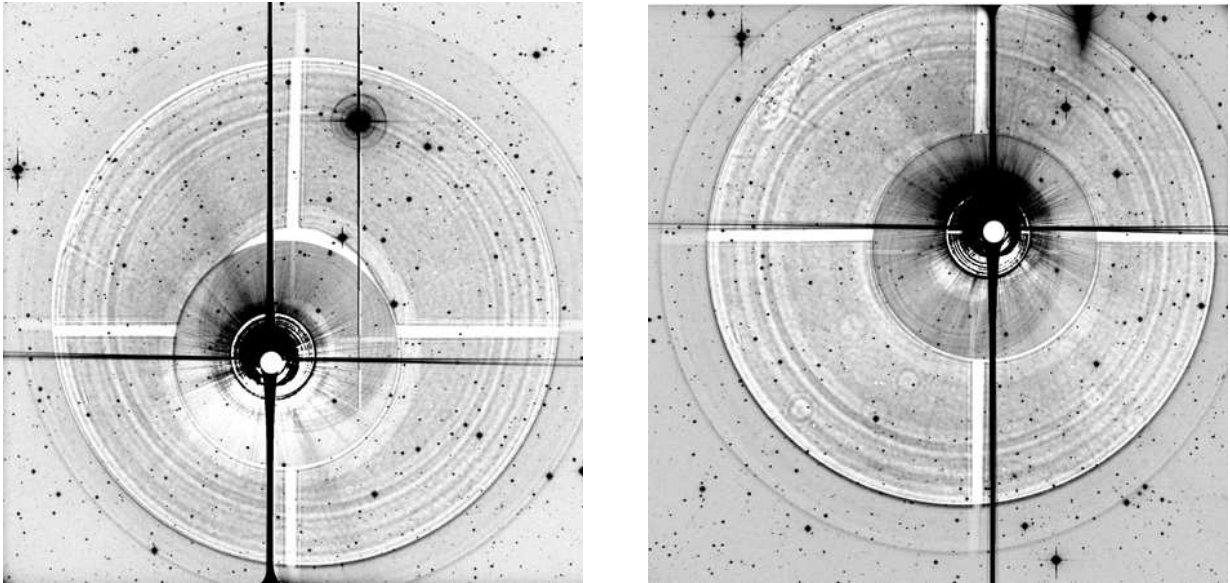


FIG. 6.— Same images as in Figure 4 after removal of the reflections and PSF. The images saturate at $\mu_V = 22.1$, roughly half the brightness of the images in Figure 4.

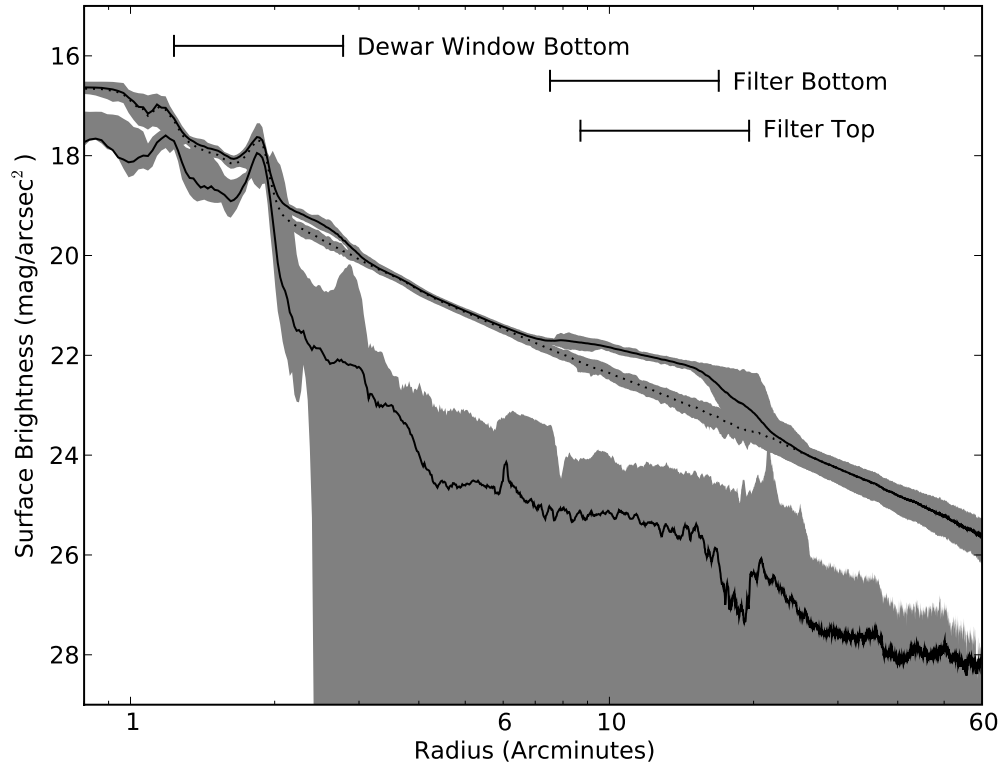


FIG. 7.— The radial profile of Arcturus in the original images (top solid line), after removing reflections (middle dotted line), and after removing both reflections and scattered light (bottom solid line). In the top two profiles the line indicates the mean of the profiles of individual images, while the bottom line is the profile of coadded image. The shaded regions indicate the maximum scatter between individual observations. The horizontal lines indicate the sizes of the reflections, although the exact area affected will vary slightly since the reflections are not concentric about the star. The read noise level for single exposures is equivalent to $27.6 \text{ mag arcsec}^{-2}$.

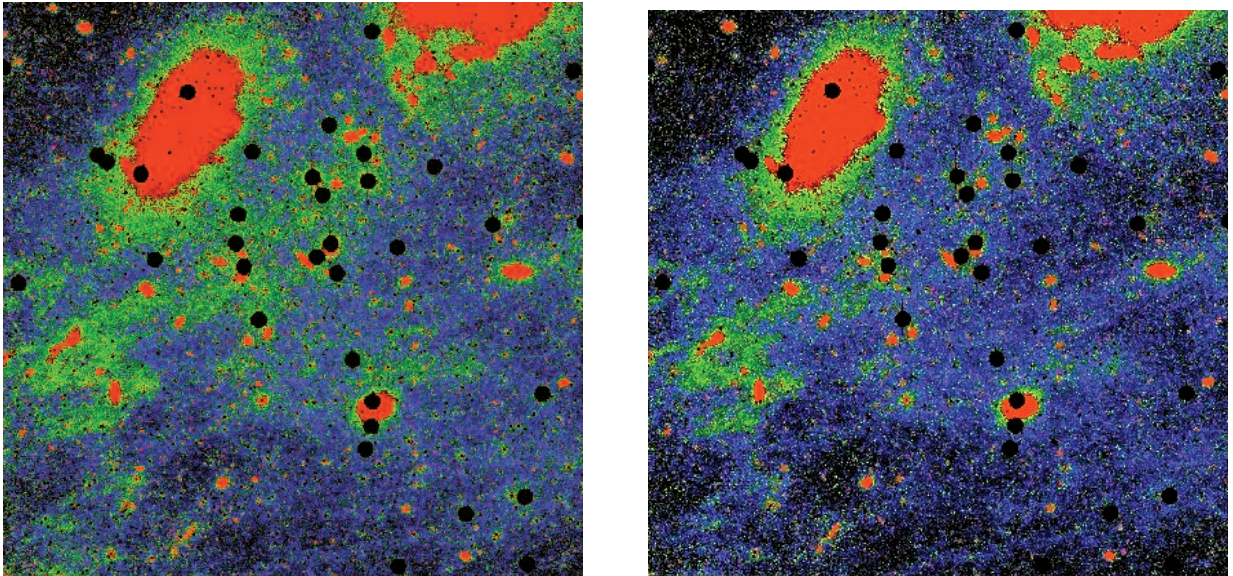


FIG. 8.— Virgo mosaic without any star subtraction is on the left, and on the right is the mosaic with full reflection modeling and star subtraction. North is up and east is to the left, and M87 is in the upper left. The mosaic is $\sim 2.5^\circ$ on each side. In both images red is $\mu_V < 27.1 \text{ mag arcsec}^{-2}$, Green is between 27.8 and 28.0, and blue is fainter than $28.0 \text{ mag arcsec}^{-2}$.

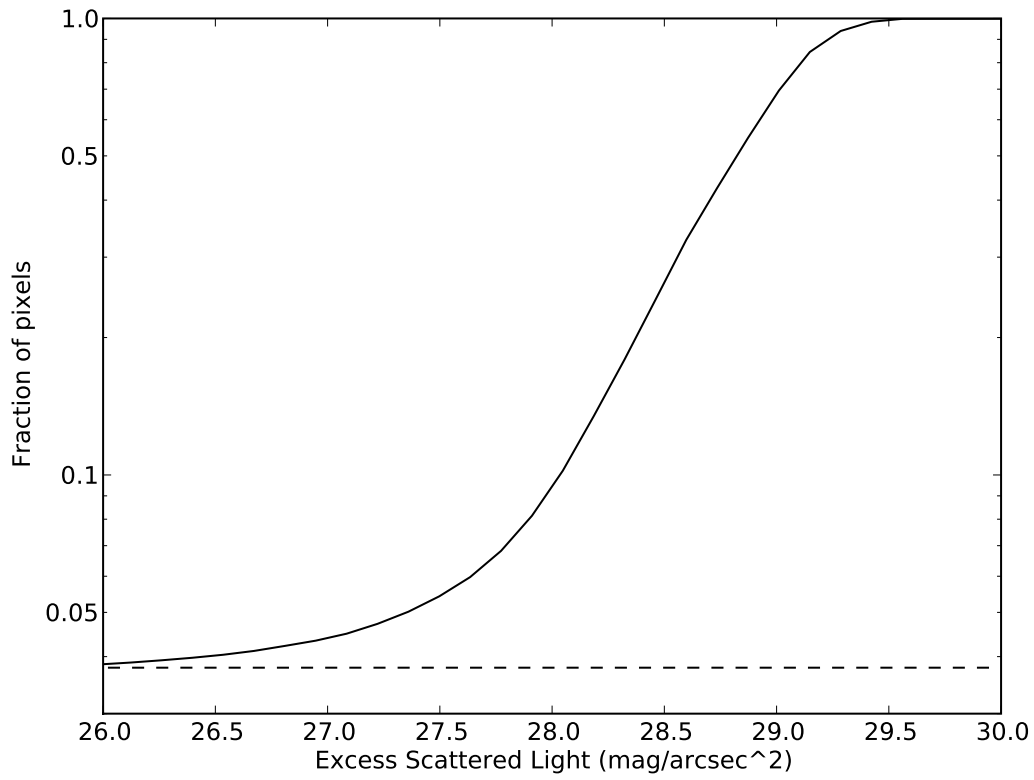


FIG. 9.— Cumulative histogram of the scattered light observed from stars in the mosaic of Virgo. The solid line indicates the fraction of pixels that received scattered light at a given surface brightness. The dashed line shows the fraction of pixels that are masked due to contamination by bright stars.

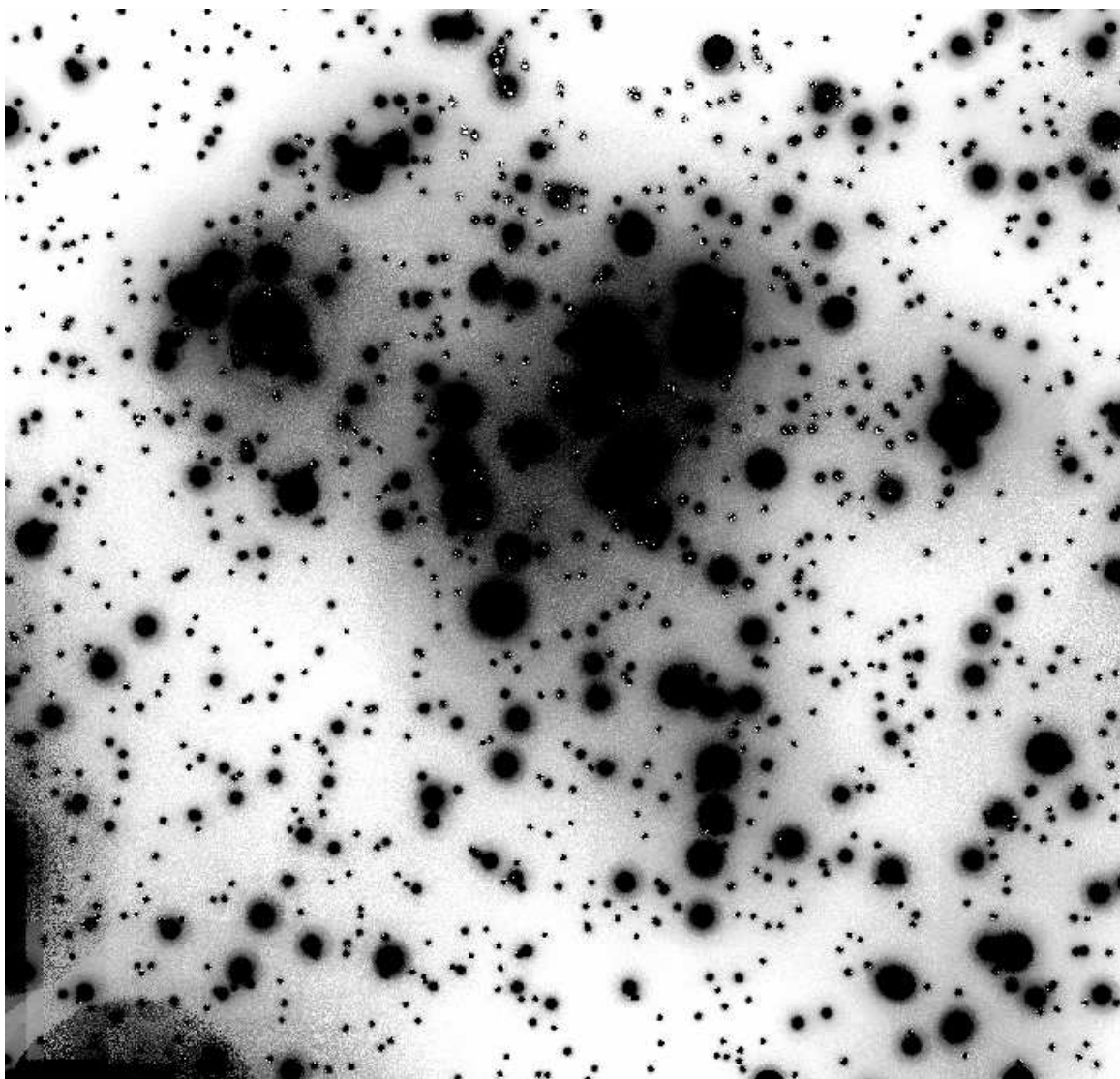


FIG. 10.— This image is the difference between the reduction with no star subtraction and the image with the fully modeled reflection and PSF subtraction. Black indicates an excess of light in the image without star subtraction, and saturates at 2.5 ADU ($\mu_V = 27.8$).

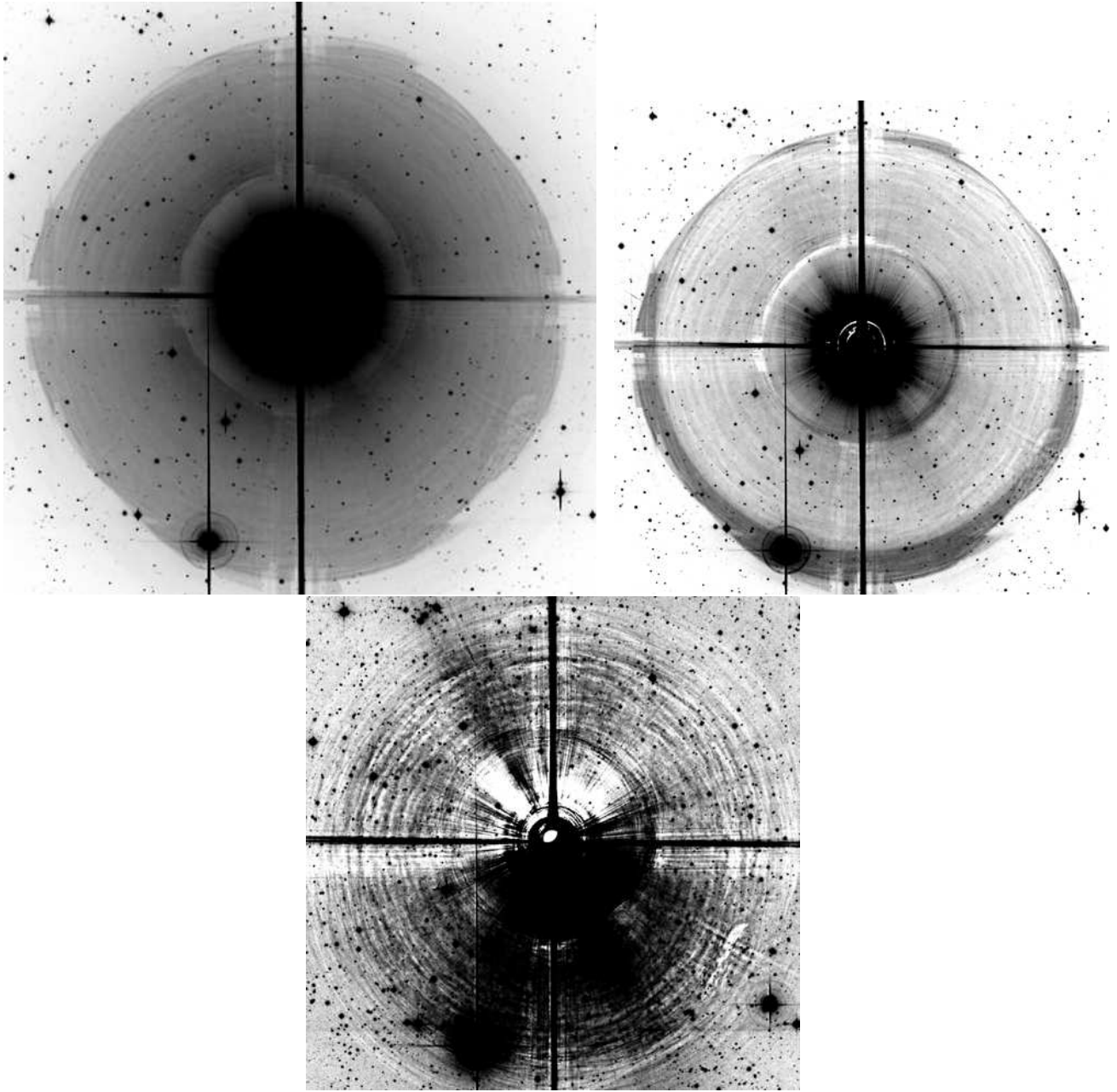


FIG. 11.— Top: Coadded mosaic of all 16 Arcturus pointings without any star subtraction. Left: Coadded mosaic after removing an average radial profile generated from a single Arcturus image. Right: Arcturus mosaic after subtracting the position-dependent PSF from each individual pointing. The top image saturates to black at 900 ADU above the background ($\mu_V = 21.5$), the left image saturates at 400 ADU ($\mu_V = 22.3$), and the right image saturates at 50 ADU ($\mu_V = 24.6$).

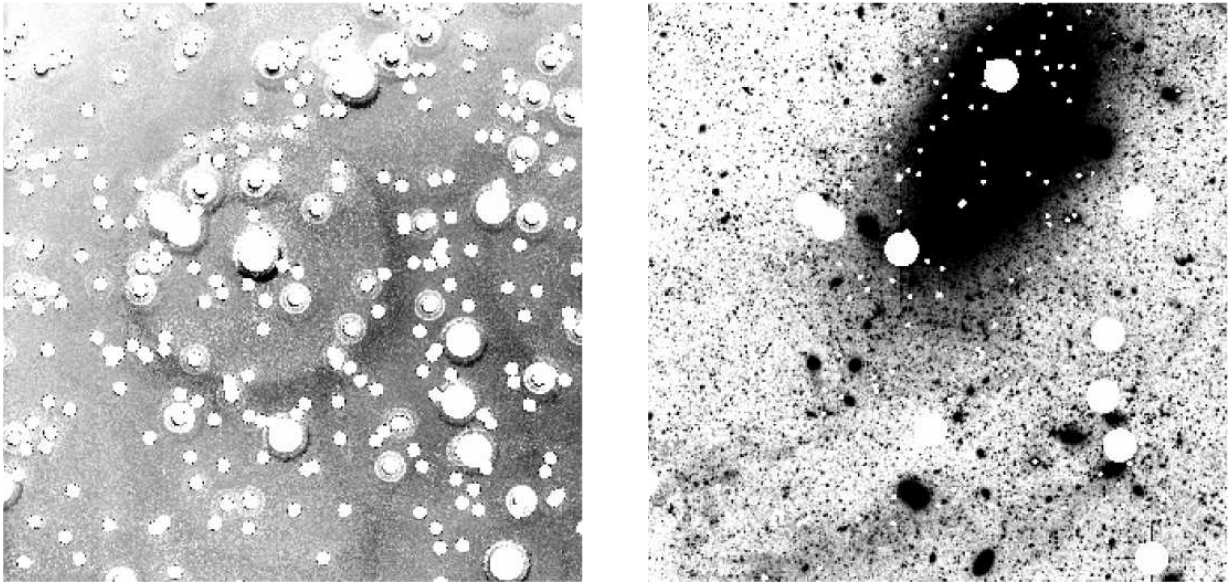


FIG. 12.— On the left is the difference between the image with exaggerated reflections that had a static PSF removed and the image with the full reflection modeling. Black in the image indicates an excess of light in the reduction with the static profile. The image saturates to black at 1.5 ADU ($\mu_V = 29.0$). On the right is the same region (showing M87) in the image with full reflection modeling.